In vivo whole-body imaging of optical agent dynamics using full angle fluorescence diffuse optical tomography

Xin Liu (刘 欣), Fei Liu (刘 飞), Daifa Wang (汪待发), and Jing Bai (白 净)*

Department of Biomedical Engineering, School of Medicine, Tsinghua University, Beijing 100084, China

**E-mail: deabj@tsinghua.edu.cn*

Received May 17, 2010

Dynamic fluorescence diffuse optical tomography (FDOT) is important in drug deliver research. In this letter, we first image the metabolic processes of micelles indocyanine green throughout the whole body of a nude mouse using the full-angle FDOT system with line illumination (L-FDOT). The resolution of L-FDOT is evaluated using phantom experiment. Next, *in vivo* dynamic tomographic images (100 frames; approximately 170 min) of mouse liver and abdomen are shown and cross-validated by planar fluorescence reflectance imaging *in vitro*. Results provide evidence on applicability of the tomographic image whole-body biological activities *in vivo* on minute timescale (approximately 1.7 min) using L-FDOT.

OCIS codes: 170.6280, 170.6960, 170.3010, 170.3880.

doi: 10.3788/COL20100812.1156.

Fluorescence diffuse optical tomography (FDOT) has been a promising optical imaging method for *in vivo* imaging of small animals. By tagging regions of interest (ROIs) with fluorescent contrast agents, FDOT allows the non-invasive and quantitative imaging of three-dimensional (3D) locations and geometries of targeted regions. FDOT has been successfully applied in oncology[1], inflammation[2], therapy[3], etc. With advances in optical contrast agents[4], imaging systems[5−8], and reconstruction algorithms[9−16], FDOT has extended its application in investigating the dynamics of optical agents in small animal *in vivo*, commonly referred to as dynamic FDOT study. By adding time as a new dimension, dynamic FDOT has offered the ability to capture the complete dynamic course of absorption, distribution, and elimination of fluorescent contrast agents, which are helpful in better studying drug delivery and disease progression.

However, challenges remain in capturing the images of fast whole-body biological activities *in vivo* utilizing FDOT, as whole body field of view, shorter scan time, and good spatial resolution should be considered simultaneously. Patwardhan *et al.* explored the use of indocyanine green (ICG) bio-distribution throughout the mouse body *in vivo* using the slab geometry-based imaging system[7]. In their reports, fast whole-body imaging was achieved by decreasing the switching time between illumination sources using galvanometer-controlled mirrors. To improve further the ability of imaging optical agent kinetics in whole body using the full-angle FDOT system, Wang *et al.* recently compared the performance of full-angle FDOT systems with different excitation patterns[8]. Based on simulation studies, they showed that the FDOT system with line illumination (L-FDOT) could better achieve whole body image qualities compared with the conventional FDOT system with point illumination when temporal resolutions remain the same. In this letter, using the L-FDOT system, we first image the metabolic processes of micelles ICG (m-ICG) at the whole-body small animal level *in vivo*. Firstly, the resolution of L-FDOT is evaluated using phantom experiment. Then *in vivo* dynamic tomographic images (100 frames; approximately 170 min) of mouse liver and abdomen are captured by employing the L-FDOT system. Finally, *in vitro* planar fluorescence reflectance imaging (FRI) is acquired to validate the reconstructed results.

The phantom and *in vivo* experimental measurements were performed in a custom-built L-FDOT imaging system. This allowed us to collect the photons propagating throughout the body of the imaged object (mouse) at 360° projections in a continuous wave (CW) mode. The sketch of the system is shown in Fig. 1. The imaged object (mouse/phantom) was suspended on a custom-built rotation stage. Two mounting stages at the top and bottom of a rigid frame were rotated identically with 6 deg./s speed to prevent possible motion from the mouse. Two sources of illumination were used to acquire fluorescence images and white light images. For fluorescence images, a small light spot from a 250-W halogen lamp (7-Star, Beijing) was converted to a narrow light beam by using a 775 ± 23-nm bandpass filter (Semrock, Rochester, USA) and a special optical fiber with one circular end and one narrow rectangular end. The light intensity distribution along the line-shaped light beam was designed as uniform. A narrow slit at the end of the optical fiber was used to fix the final narrow light beam on the mouse at less than 0.1-cm width and over 4.0-cm height. The length of the final excitation beam depended on the imaged object. The final excitation beam should be efficient enough to illuminate the imaged object while avoiding direct transmission of excitation light to the charge-coupled device (CCD). To acquire surface silhouettes, which were used to recover the 3D geometry of the imaged object, a white light bulb was placed in front of the imaged object while the halogen lamp was switched off. The photons propagating through the imaged object were detected by a 14-bit electron multiplying CCD (EMCCD) camera (Andor, Belfast, Northern Ireland) cooled to −70 °C to reduce dark noise, and a 60-mm $f/2.8D$ lens (Nikon, Melville, USA). In collecting fluorescence images, the 840 ± 6-nm bandpass filter (Semrock, Rochester, USA) was placed in front of the lens. In

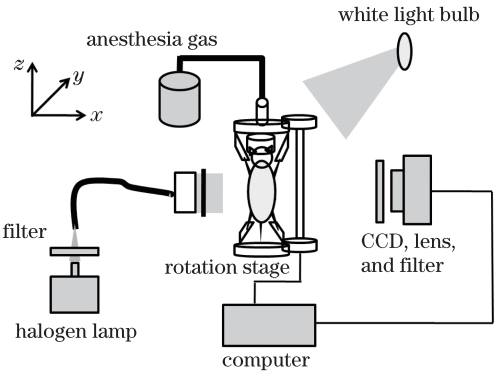

Fig. 1. Experimental setup.

collecting excitation images, a neutral density filter (Daheng, Beijing) with 1% transmittance was placed in front of the lens to prevent possible highlight damage to the EMCCD. In collecting white light images, the white light bulb was switched on to provide front light illumination while the excitation light was switched off.

Tomographic image reconstructions were performed using the normalized Born method[9], as this corrects the influences of heterogeneity on mouse tissues. The normalized ratio of the emission (fluorescence) measurements $\Phi_{\rm m}(\mathbf{r}_{\rm d})$ and the corresponding excitation measurements $\Phi_{\rm x}(\mathbf{r}_{\rm d})$ at detector point $\mathbf{r}_{\rm d}$ is given as

$$\frac{\Phi_{\rm m}(\mathbf{r}_{\rm d})}{\Phi_{\rm x}(\mathbf{r}_{\rm d})} = \Theta \frac{\int_V G_{L(\mathbf{r})}(\mathbf{r}_p) G_{\delta(\mathbf{r}-\mathbf{r}_{\rm d})}(\mathbf{r}_p) n(\mathbf{r}_p) {\rm d}\mathbf{r}_p}{G_{L(\mathbf{r})}(\mathbf{r}_{\rm d})}, \quad (1)$$

where $\mathbf{r}_p$ is the point inside volume V considered for reconstruction; $n(\mathbf{r}_p)$ is the fluorescence yield at point $\mathbf{r}_p$, which is directly proportional to the concentration of the fluorophores; $G_{\delta(\mathbf{r}-\mathbf{r}_{\rm d})}(\mathbf{r}_p)$ denotes the Green's function value at $\mathbf{r}_p$ due to point source $\delta(\mathbf{r}-\mathbf{r}_{\rm d})$ at $\mathbf{r}_{\rm d}$; Θ is a calibration factor accounting for the unknown gain and attenuation factors of the system, such as excitation light power; $G_{L(\mathbf{r})}(\mathbf{r}_p)$ denotes the Green's function value at $\mathbf{r}_p$ due to the line excitation source term $L(\mathbf{r})$, which is defined as

$$L(\mathbf{r}) = \begin{cases} \int_{\{\mathbf{r}_{\rm l}\}} L(\mathbf{r}) {\rm d}\mathbf{r} = 1 \\ L(\mathbf{r}_1) = L(\mathbf{r}_2) \quad \mathbf{r}_1, \mathbf{r}_2 \in \{\mathbf{r}_{\rm l}\} \\ L(\mathbf{r}) = 0 \qquad\qquad \mathbf{r} \notin \{\mathbf{r}_{\rm l}\} \end{cases}, \quad (2)$$

where $\mathbf{r}_1$ is the point on the line $\{\mathbf{r}_1\}$. When volume V is sampled in voxels, a linear system $\Phi_{\rm m}/\Phi_{\rm x} = \mathbf{W}n$ is generated for all source-detector pairs based on Eq. (1). The unknown fluorescence value n in each voxel was calculated by inverting weight matrix $\mathbf{W}$ with an algebraic reconstruction technique (ART) with non-negative constraints.

Phantom experiment was first conducted to evaluate the performance of the L-FDOT system. As shown in Fig. 2(a), two transparent glass tubes (0.3 cm in diameter) filled with 1.3-μmol/L ICG were immersed in

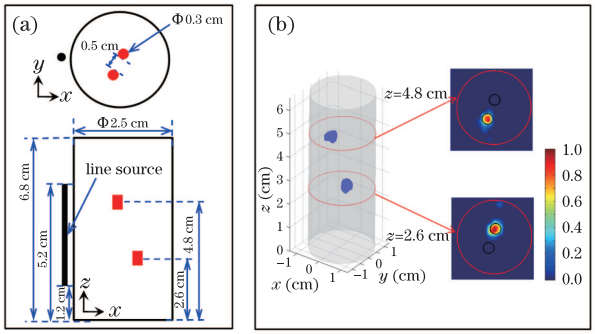

Fig. 2. Spatial resolution of L-FDOT. (a) Phantom experimental configuration. Two glass tubes (0.3 cm in diameter) filled with 1.3-μmol/L ICG are placed in a 2.5-cm diameter cylinder phantom at the heights of 2.6 and 4.8 cm, respectively, and with an edge-to-edge distance of 0.5 cm. (b) Reconstructed results of two fluorescent tubes. Outer circles on the cross section images depict the actual phantom boundary; small circles on the cross section images depict the actual tubes. Both reconstructed images are normalized to the maximum value.

a cylinder phantom. The phantom was made of a glass cylinder (2.5 cm in diameter) filled with 1% intralipid (reduced scattering coefficient $\mu_{\rm s}'$=10.0 cm^{-1}, absorption coefficient $\mu_{\rm a}$=0.02 cm^{-1}). The two tubes were separated by an edge-to-edge distance of 0.5 cm and height difference of 2.2 cm along the z axis. In the experiment, 36 excitation and emission images were collected in 10 ° steps. In the reconstruction, the detectors were fixed on the boundary finite element nodes (4.3 cm in height range) and inside the 160 ° field of view of the corresponding line source. The reconstruction mesh was $2.5 \times 2.5 \times 6.8$ (cm) in the 3D region with 0.1-cm spacing. Only the mesh inside the imaged object was considered for reconstruction. Reconstructions were terminated after 100 ART iterations. The reconstructed results are shown in Fig. 2(b). The two tubes placed at different heights were sufficiently localized and quantified with only one cycle of projections, as opposed to conventional FDOT imaging systems with point illumination. As a result, based on the line illumination, the whole-body FDOT data acquisition time was reduced and the time resolution of imaging whole-body fluorescent marker distributions was improved, which are beneficial to image dynamic metabolic processes.

For imaging metabolic processes *in vivo* of m-ICG throughout the body of a small animal, a nude mouse (6 weeks, 20 g) was anesthetized with an isoflurane veterinary vaporizer (Matrx, New York, USA). After being suspended on the rotation stage, the mouse was injected on its tail vein with 0.2-mL m-ICG (25.8 nmol). Subsequently, the mouse was continuously rotated in 100 cycles to capture the m-ICG metabolic processes throughout its body. For each cycle, 18 fluorescence images (2-s exposure time and 4×4 CCD binning) were obtained in 20° steps. The total power delivered on mouse surface was about 4 mW. After imaging, 18 excitation light images (0.8-s exposure time and 1×1 CCD binning) were acquired and used to correct the highly heterogeneous attenuation of the tissues. Finally, 72 white light images acquired in 5° steps were back-projected to form a 3D geometry of the mouse[17]. One cycle of fluorescence projection took approximately 1.7 min, depending on the

sum of rotation time and total exposure time of images. The total imaging time was approximately 170 min. Throughout the experiment, anesthesia was maintained with isoflurane-air gas mixture.

Before reconstructing the distribution of fluorescence contrast agents, fluorescence signals were normalized using Eq. (1) to correct the high degree of light scattering in the tissue *in vivo*. The comparison between raw fluorescence images and normalized fluorescence images is shown in Fig. 3. The first and third rows of Fig. 3 depict normalized fluorescence images from the body of the mouse at different time points (1.7, 19, 36, 53, 104, and 170 min) captured at 180° and 300° projections. In contrast, the corresponding raw fluorescence images are shown in the second and fourth rows in Fig. 3. As shown in the figures, the areas of the highest light intensity are at the side edges of the mouse, mainly due to heterogeneous influences of tissue and excitation light "bleed-through". Compared with raw fluorescence images, the normalized images enhanced the contrast of true fluorescence distribution.

For the reconstruction at each cycle (frame), the detectors were fixed onto the boundary finite element nodes, which were at 4.5-cm height range and inside 160° field of view of the corresponding line source. The volume considered for reconstruction was $3.0 \times 4.0 \times 4.5$ (cm) and sampled to $19 \times 26 \times 29$ voxels. The 2872 voxels inside the object were used for reconstruction. The number of ART iterations was fixed to 10. Several relaxation parameters have been tested by Herman *et al.*[18] In the following reconstructions, we used the value 0.1 for the relaxation parameter λ. These parameters have been used as generic values similar to previous experiments. More rigorous convergence criteria can be employed, but their selection is also generally based on the quality of

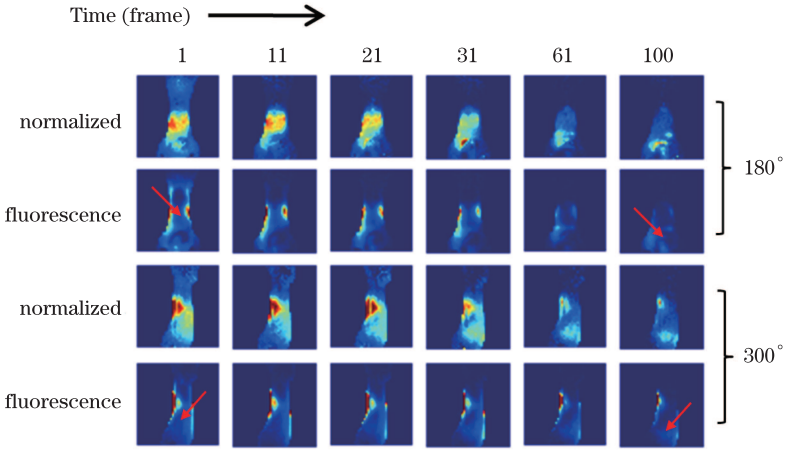

Fig. 3. Comparison between the fluorescence images and the normalized fluorescence image. The first and third rows depict normalized fluorescence images from the whole body of mouse at different frames (1, 11, 21, 31, 61, and 100) corresponding to different time points (1.7, 19, 36, 53, 104, and 170 min) captured at 180° and 300° projections. The corresponding raw fluorescence images are depicted in the second and fourth rows.

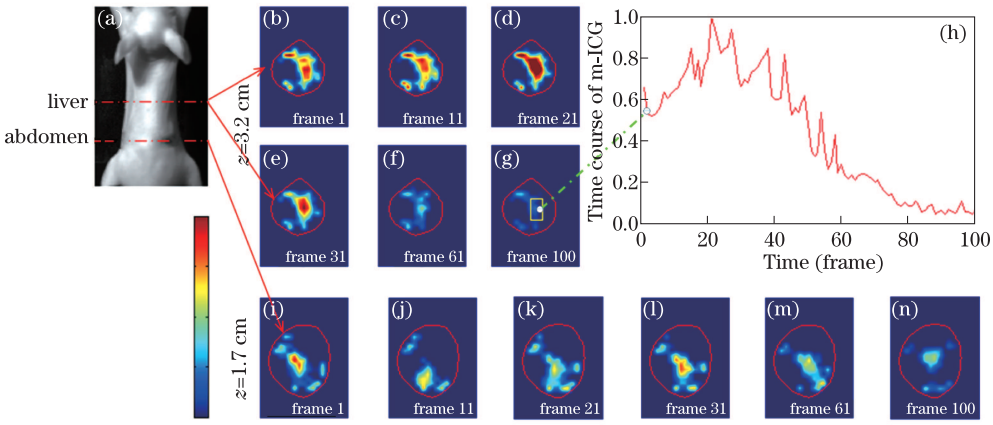

Fig. 4. Bio-distribution of m-ICG in organs after tail vein injection. (a) White light image at 0°. (b)–(g) Dynamic reconstructed images at frame 1 (1.7 min), frame 11 (19 min), frame 21 (36 min), frame 31 (53 min), frame 61 (104 min), and frame 100 (170 min) captured at z=3.2 cm. (i)–(n) Dynamic tomographic images at z=1.7 cm using the abovementioned time points. All tomographic images are displayed at the same range. (h) The time course of m-ICG in the ROI of liver, depicted using rectangle in (g). The x axis represents time (frames), and the y axis represents mean value of ROI. The obtained mean value is normalized to its maximum value. Curves on (b)–(g) and (i)–(n) show the actual surface of mouse for different height slices, depicted with the dashed lines in (a).

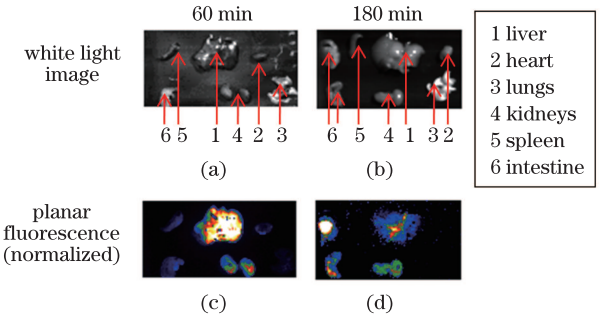

Fig. 5. *In vitro* planar fluorescence images. (a), (b) White light images of major organs of mouse (heart, liver, lungs, spleen, kidneys, and intestine) at 60 and 180 min; (c), (d) normalized planar fluorescence images of the corresponding organs at 60 and 180 min.

the reconstructed images. The results of the tomographic reconstructions (1.7, 19, 36, 53, 104, and 170 min) using the normalized data are shown in Fig. 4.

Figures 4(b)–(g) illustrate the m-ICG kinetics in the liver (z=3.2 cm). Figures 4(i)–(n) illustrate the m-ICG kinetics in the abdomen (z=1.7 cm). The bio-distribution of m-ICG initially accumulated in the liver. Using anatomical structure and the two-dimensional (2D) reconstruction slices as guides, the ROI corresponding to the liver was selected (see the rectangle in Fig. 4(g)). Subsequently, the mean concentrations of m-ICG in the ROI were calculated for all time points. Figure 4(h) shows the time course of m-ICG kinetics in the ROI. The results suggest that the bio-distribution of m-ICG in the liver initially increases. After 36 min (frame 21), the bio-distribution gradually decreased.

To aid in validating the reconstructed results, the fluorescence intensities of the major organs (heart, liver, lungs, spleen, kidneys, and intestine) *in vitro* at 60 and 180 min were acquired and used. Two mice injected with the same dose of m-ICG through the tail vein were euthanized, dissected, and imaged utilizing planar FRI. *In vitro* reflectance images of the major organs at 60 and 180 min are shown in Fig. 5. As shown in Fig. 5(c), at 60 min, the bio-distribution of m-ICG in the liver is significantly stronger than the bio-distribution in other organs. This was consistent with the reconstructed bio-distribution of m-ICG in the liver (Fig. 4(e)) and the abdomen (Fig. 4(l)) at about 53 min (frame 31). Similarly, in Fig. 5(d), the bio-distribution of m-ICG in the liver is lower than the bio-distribution in the intestine at 180 min. The trend corresponded with the reconstructed results in Figs. 4(g) and (n) wherein the bio-distribution of m-ICG in liver (Fig. 4(g)) is lower than that in the abdomen (Fig. 4(n)) at about 170 min.

In conclusion, using L-FDOT, we have conducted tomographic imaging of fast whole-body biological activities *in vivo* at the minute timescale of approximately 1.7 min. This provides for a promising application in studying drug delivery, disease progression, protein metabolism, etc. However, in this letter, reconstruction is performed using the normalized Born method. The method cannot completely eradicate the influence of tissue heterogeneity, which may lead to reconstructed errors, especially in *in vivo* experiments. Moreover, as the actual anatomical information of organs is unknown, the accuracy of the reconstructed results cannot be further validated. Further research wiu focus on the use of anatomical information provided by micro computed tomography[19] in order to improve the reconstruction quality[14] and to validate the accuracy of the reconstructed results.

We gratefully thank Prof. Wei Liang for providing the m-ICG. This work was supported by the National Natural Science Foundation of China (Nos. 81071191, 30670577, 60831003, 30930092, and 30872633), the Tsinghua-Yue-Yuen Medical Science Foundation, the National Basic Research (973) Program of China (No. 2011CB707701), and the National High-Tech Research and Development (863) Program of China (No. 2006AA020803).

References

1. A. Corlu, R. Choe, T. Durduran, M. A. Rosen, M. Schweiger, S. R. Arridge, M. D. Schnall, and A. G. Yodh, Opt. Express **15,** 6696 (2007).
2. J. Haller, D. Hyde, N. Deliolanis, R. de Kleine, M. Niedre, and V. Ntziachristos, J. Appl. Physiol. **104,** 795 (2008).
3. V. Ntziachristos, E. A. Schellenberger, J. Ripoll, D. Yessayan, E. Graves, A. Bogdanov, L. Josephson, and R. Weissleder, PNAS **101,** 12294 (2004).
4. X. Michalet, F. F. Pinaud, L. A. Bentolila, J. M. Tsay, S. Doose, J. J. Li, G. Sundaresan, A. M. Wu, S. S. Gambhir, and S. Weiss, Science **307,** 538 (2005).
5. G. Hu, J. Yao, and J. Bai, Prog. Nat. Sci. **18,** 707 (2008).
6. N. Deliolanis, T. Lasser, D. Hyde, A. Soubret, J. Ripoll, and V. Ntziachristos, Opt. Lett. **32,** 382 (2007).
7. S. V. Patwardhan, S. R. Bloch, S. A. Achilefu, and J. P. Culver, Opt. Express **13,** 2564 (2005).
8. D. Wang, X. Liu, and J. Bai, Opt. Express **17,** 21376 (2009).
9. A. Soubret, J. Ripoll, and V. Ntziachristos, IEEE Trans. Med. Imaging **24,** 1377 (2005).
10. X. Song, D. Wang, and J. Bai, Opt. Express **15,** 18300 (2007).
11. F. Gao, L. Zhang, J. Li, and H. Zhao, Chin. Opt. Lett. **6,** 889 (2008).
12. C. Qin, J. Tian, X. Yang, K. Liu, G. Yan, J. Feng, Y. Lv, and M. Xu, Opt. Express **16,** 20317 (2008).
13. X. Liu, D. Wang, F. Liu, and J. Bai, Opt. Express **18,** 6300 (2010).
14. D. Hyde, E. L. Miller, D. H. Brooks, and V. Ntziachristos, IEEE Trans. Med. Imaging **29,** 365 (2010).
15. L. Zhang, H. He, F. Gao, and H. Zhao, Acta Opt. Sin. (in Chinese) **28,** 1262 (2008).
16. L. Zhang, F. Gao, J. Li, and H. Zhao, Chinese J. Lasers (in Chinese) **36,** 2552 (2009).
17. D. Wang, X. Liu, Y. Chen, and J. Bai, Chin. Opt. Lett. **8,** 82 (2010).
18. G. T. Herman and L. B. Meyer, IEEE Trans. Med. Imaging **12,** 600 (1993).
19. H. Li, H. Zhang, Z. Tang, and G. Hu, Prog. Nat. Sci. **18,** 513 (2008).